Quiet-Zone Evaluation Using a Spherical Synthetic-Aperture Radar

Ronald C. Wittmann
National Institute of Standards and Technology
325 Broadway, Boulder, CO 80303-3328

Donald N. Black
EMS Technologies, Inc.
P. O. Box 7700, Norcross, GA 30091-7700

1 Introduction

A compact range, for example, will never produce a perfect plane wave in the target zone. Knowledge of the actual incident field is essential for assessing and/or improving measurement quality. In this paper we use quiet-zone illumination data to produce a synthetic-aperture image of a microwave measurement range [1], [2], allowing isolation and physical removal of unwanted signal sources. We discuss recent results concerning resolution, dynamic range, and focusing in such images, and some experimental data are presented.

To obtain illumination data, we use a known probe (on a roll-over-azimuth mount) to make measurements on a spherical surface. (Thus, standard positioners can be used and special linear probing devices are not required.) These data can be processed to determine the incident field within the volume of the sphere [3]. The technique is closely related to well-known spherical near-field scanning algorithms for determining antenna radiation patterns [4]. In contrast to common field probing practices, which give qualitative estimates, the present method will produce, in principle, an accurate incident field reconstruction that has been fully compensated for probe pattern effects.

2 Quiet-Zone Fields

Within a spherical volume, $r < r_0$, containing no sources, the electric field may be written [1]

$$\mathbf{E}(\mathbf{r}) = \frac{1}{4\pi} \int_0^{2\pi} d\phi' \int_0^{\pi} \sin\theta' \, d\theta' \mathbf{a}\left(\hat{\mathbf{k}}'\right) \exp\left(i\mathbf{k}' \cdot \mathbf{r}\right) \, d\hat{\mathbf{k}}', \tag{1}$$

The spectrum $\mathbf{a}(\hat{\mathbf{r}})$ is

$$\mathbf{a}(\hat{\mathbf{r}}) \approx \sum_{n=1}^{N} \sum_{m=-n}^{n} \left[a^1_{nm} \mathbf{X}_{nm}(\hat{\mathbf{r}}) + a^2_{nm} \mathbf{Y}_{nm}(\hat{\mathbf{r}}) \right], \tag{2}$$

where $\mathbf{X}_{nm}$ and $\mathbf{Y}_{nm} \equiv i\hat{\mathbf{r}} \times \mathbf{X}_{nm}(\hat{\mathbf{r}})$ are (vector) spherical harmonics, and carets mark unit vectors. The expansion (2) is typically truncated at $n = N \sim kr_0$. The magnetic and electric multipole coefficients a^1_{nm} and a^2_{nm} are determined from probe data gathered on the surface $r = r_0$.

U.S. Government Work Not Protected by U.S. Copyright

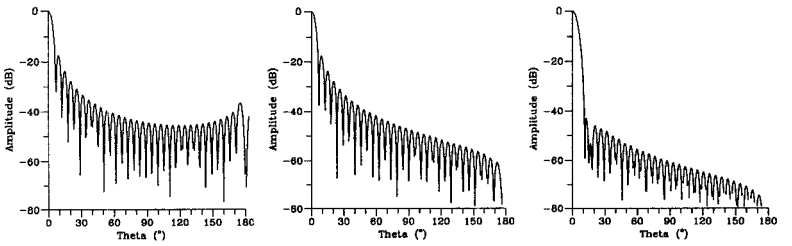

(a) $D_{32}(\theta)$ (b) $D_{32}^{a}(\theta)$ (c) $D_{32}^{b}(\theta)$

Figure 1:

3 Imaging a Range

An image can be formed by plotting the amplitude of the spectrum as a function of $\hat{\mathbf{r}}$. For example, as implied by (1), the spectrum of a plane wave behaves as a Dirac delta function. Consequently, the image of an incident plane wave will be focused at $\hat{\mathbf{r}} = \hat{\mathbf{k}}$, where $\hat{\mathbf{k}}$ is the direction of propagation. Similarly, the images of distant objects will be sharply focused. On the other hand, the images of nearby objects will be broadened (out of focus) according to the spectral content of their radiated (scattered) fields.

In order to make this discussion quantitative, we note that the spectrum of the plane wave $\boldsymbol{\kappa} \exp(i\mathbf{k}\cdot\mathbf{r})$ is

$$\mathbf{a}(\hat{\mathbf{r}}) \approx 4\pi \sum_{nm}^{N} \begin{bmatrix} \mathbf{X}_{nm}(\hat{\mathbf{r}})\,\mathbf{X}_{nm}^{*}\left(\hat{\mathbf{k}}\right) \\ +\mathbf{Y}_{nm}(\hat{\mathbf{r}})\,\mathbf{Y}_{nm}^{*}\left(\hat{\mathbf{k}}\right) \end{bmatrix} \cdot \boldsymbol{\kappa} = 4\pi \underline{\boldsymbol{\delta}}_{N}\left(\hat{\mathbf{r}}, \hat{\mathbf{k}}\right) \cdot \boldsymbol{\kappa}.$$

(The polarization vector $\boldsymbol{\kappa}$ satisfies $\hat{\mathbf{k}} \cdot \boldsymbol{\kappa} = 0$ and $|\boldsymbol{\kappa}| = 1$.) Thus, the image of a plane wave or a distant point source is proportional to the point-spread function

$$D_N(\theta) \equiv \left| 4\pi \underline{\boldsymbol{\delta}}_{N}\left(\hat{\mathbf{r}}, \hat{\mathbf{k}}\right) \cdot \boldsymbol{\kappa} \right|. \tag{3}$$

We find that

$$\begin{aligned} D_N(\theta) &= \left(\frac{1+\cos\theta}{2}\right) \left| \sum_{n=1}^{N} (2n+1)\, P_{n-1}^{(0,2)}(\cos\theta) \right| \\ &= (N+2) \left(\frac{1+\cos\theta}{2}\right) \left| P_{N-1}^{(1,2)}(\cos\theta) \right|, \end{aligned} \tag{4}$$

where the $P_n^{(\alpha,\beta)}$ are Jacobi polynomials. We emphasize that D_N depends only on $\cos\theta \equiv \hat{\mathbf{k}} \cdot \hat{\mathbf{r}}$ and, in particular, is independent of $\boldsymbol{\kappa}$. As an example, we plot $D_{32}(\theta)$ in figure 1a.

4 Resolution and Dynamic Range

The asymptotic formula

$$\lim_{N\to\infty} \frac{1}{N} P_N^{(1,2)}\left[\cos\left(\frac{z}{N}\right)\right] = \frac{J_1(z)}{z/2}$$

allows estimation of the resolution $\Delta\theta$ (the angle from the peak to the first 0) and the level of the first sidelobe ΔP

$$\Delta\theta \sim \frac{3.83}{N} \tag{5}$$

$$\Delta P \sim 20\log\left|\frac{J_1(5.14)}{5.14/2}\right| \approx -17.6 \text{ dB}. \tag{6}$$

Here, 3.83171 and 5.13652 approximate the first positive 0's of the Bessel functions J_1 and J_2. These parameters also characterize the on-axis response of plane-circular aperture of radius $r_0 = N/k$. Equations (5) and (6) can be used to analyze figure 1a.

It is easy to reduce the amplitude near $\theta = \pi$. Consider

$$\begin{aligned} D_N^a(\theta) &= (N+2)\left(\frac{1+\cos\theta}{2}\right)\frac{N-1}{2N}\left|P_{N-1}^{(1,2)} + \frac{N+1}{N-1}P_{N-2}^{(1,2)}\right| \\ &= (N+2)\left(\frac{1+\cos\theta}{2}\right)^2\left|P_{N-2}^{(1,3)}(\cos\theta)\right|. \end{aligned} \tag{7}$$

In (7) the sum of the Jacobi polynomials is 0 at $\theta = \pi$. The point-spread function D_N^a arises when the simple window function

$$w_n^a = \begin{cases} 1, & n < N \\ (N-1)/2N, & n = N \end{cases}$$

is applied to (4), that is, when the Nth term is weighted by approximately 1/2. In figure 1b, we plot D_{32}^a to show the decrease in level for $\theta > \pi/2$.

Close-in sidelobes may also be reduced by windowing. If we employ the window $w_n^a w_n^b$ in (4), where

$$w_n^b \equiv 0.54 + 0.46\cos\left(\frac{\pi n}{N}\right),$$

we obtain the point-spread function D_N^b plotted in figure 1c. Here all sidelobes are below -40 dB relative to the peak. The tradeoff between resolution and dynamic range is evident on comparing sidelobes and main beamwidths in figures 1b and 1c.

5 Experimental Results

Measurements used to verify the range imaging technique were made at the Georgia Institute of Technology spherical near-field range.[2] For our test, the incident field consists of a primary (approximately plane-wave) illumination source at $\theta = 0°$ and an "unwanted" secondary source (a metal plate) centered at $\theta = 98°$. The angular extent of the secondary source is about 17°. The summation in (2) is truncated at $N = 43 \approx kr_0$. A detailed account of the range and the measurement is given in [5]. A constant ϕ cut of the range image [spectrum, see (2)] is plotted in figure 2a.

In this case, ϕ is chosen so the cut passes though the center of the secondary source. The secondary source image peaks at $\theta = 108°$ at about 13 dB below the primary source image maximum. (Apparently, the specular point is near the physical edge of the plate.) As determined from the image of the primary source, resolution

[2]This work supported by the Joint Services Electronics Program under contract DAAL-03-09-C-0004.

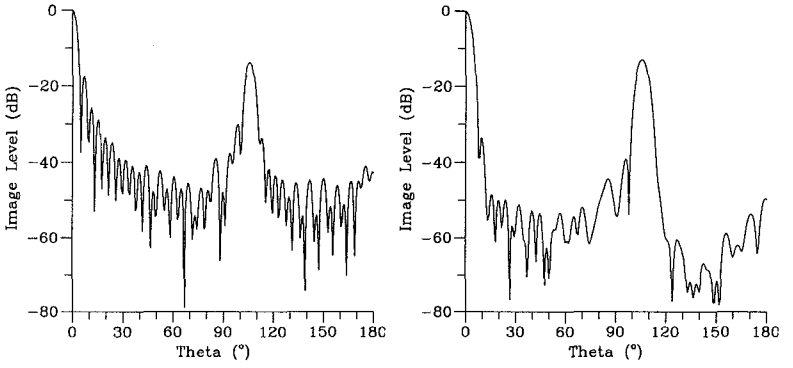

Figure 2: Images of the Georgia Institute of Technology spherical near-field range

is $\Delta\theta = 4.9°$ [agreeing well with $\Delta\theta = 5.1°$ from (5)], and the first sidelobe peaks at $\Delta P = -17.5$ dB [compared with $\Delta P = -17.6$ dB from (6)]. The range image was windowed using $w_n^a w_n^b$, and the result is given in figure 2b (for the same cut used in figure 2a). The secondary source image still peaks at 108°, but the maximum has increased by about 0.5 dB. This is in contrast to a significant decrease in the background. Both the primary and secondary source images have broadened, as expected for this type of window.

6 Summary

We have presented a spherical synthetic-aperture technique for imaging antenna/ RCS ranges. We have shown how resolution depends on the radius of the spherical measurement surface and have applied window functions to increase image contrast at the expense of resolution. Currently we are evaluating focusing techniques that could improve performance at specific source distances. Some aspects of the method were demonstrated using measured data.

References

[1]R. C. Wittmann, and D. N. Black, *Proc. AMTA*, Seattle, pp. 406–410, 1990.

[2]D. N. Black, E. B. Joy, M. G. Guler, R. E. Wilson, and G. Edgar, *Proc. AMTA*, Philadelphia, pp. 14-19–14-23, 1990.

[3]R. C. Wittmann, *1990 IEEE Antennas and Propagation Symposium Digest*, pp. 224-227, 1990.

[4]*Spherical Near-Field Antenna Measurements*, J. E. Hansen, ed. London: Peregrinus, 1988.

[5]D. N. Black, E. B. Joy, J. W. Epple, M. G. Guler, and R. E. Wilson, *Proc. AMTA*, Dallas, pp. 239–243, 1993.